

# Discovery of a pulsating Fe K $\alpha$ line in GX 301-2

Jiren Liu<sup>1\*</sup>, Roberto Soria<sup>2,3,4</sup>, Erlin Qiao<sup>1,2</sup>, and Jifeng Liu<sup>1,2</sup>

<sup>1</sup>National Astronomical Observatories, 20A Datun Road, Beijing 100012, China

<sup>2</sup>College of Astronomy and Space Sciences, University of Chinese Academy of Sciences, Beijing 100049, China

<sup>3</sup>International Centre for Radio Astronomy Research, Curtin University, GPO Box U1987, Perth, WA 6845, Australia

<sup>4</sup>Sydney Institute for Astronomy, School of Physics A28, The University of Sydney, Sydney, NSW 2006, Australia

Accepted XXX. Received YYY; in original form ZZZ

## ABSTRACT

We report on the detection of a pulsating Fe K $\alpha$  line in the High Mass X-ray Binary (HMXB) GX 301-2, from a 40-ks *Chandra* observation near periastron. The pulsations in the Fe K $\alpha$  emission appeared only in the first 7 ks of the observation, with a period and phase profile similar to those of the continuum. The presence of pulsed fluorescent lines is an unusual property in HMXBs. After 7 ks, the continuum flux increased by a factor of three, the Fe K $\alpha$  flux increased only by about 10%, and the pulsating signal in the line disappeared. Finally, in the second half of the observation, both the continuum and the line flux dropped by a similar factor of 2. We suggest that the pulsating component of the Fe K $\alpha$  line is coming from a transient non-isotropic distribution of dense gas around the neutron star, for example an accretion stream induced by periastron passage, or from the illuminated surface of the donor star.

**Key words:** pulsars: individual: GX 301-2 - X-rays: binaries

## 1 INTRODUCTION

The classical High Mass X-ray Binary (HMXB) system GX 301-2 consists of a pulsar immersed in a slow ( $\approx 300$  km s<sup>-1</sup>) and dense stellar wind ( $\dot{M}_w \sim 10^{-5} M_\odot$  yr<sup>-1</sup>), arising from the B1 hypergiant Wray 977 (Kaper et al. 2006). The donor star has an estimated mass of  $\approx 39$ – $53 M_\odot$ , a radius of  $\approx 62 R_\odot$ , and a distance from us of  $\approx 3$  kpc (Kaper et al. 2006). The orbit of the pulsar has a period  $P_{\text{orb}} = 41.506 \pm 0.003$  d, with reference phase 0 at the Modified Julian Date (MJD)  $T_0 = 43,906.06 \pm 0.11$ , and an orbital period derivative estimated as  $\dot{P}_{\text{orb}} = (-3.7 \pm 0.5) \times 10^{-6}$  s s<sup>-1</sup> (Doroshenko et al. 2010). The system has an eccentricity  $e \approx 0.46$ , with a periastron distance of  $\approx 25 R_\odot$  between the neutron star and the surface of the donor star (Sato et al. 1986; Koh et al. 1997). The inclination angle is moderately high, between  $44^\circ$ – $78^\circ$  (Leahy & Kostka 2008; Kaper et al. 2006). The pulsar has a long spin period  $P_s \approx 680$  s, which showed erratic changes over the last 30 years (e.g. Doroshenko et al. 2010; Evangelista et al. 2010). Such a long pulse period has been attributed to a strong magnetic field ( $\sim 10^{14}$  G, Doroshenko et al. 2010). The field measured from the cyclotron line is much weaker ( $\approx 5 \times 10^{12}$  G), but the two values can be consistent with each other if the cyclotron line region comes from a tall accretion column of height  $\approx 2.5$ – $3 R_{NS}$

(Doroshenko et al. 2010, but also see Ikhsanov & Finger (2012)).

The X-ray continuum flux of GX 301-2 shows regular orbital modulations and reaches a maximum about 1.4 days before periastron passage (Sato et al. 1986). The flux increase has been explained by a gas stream induced by the neutron star near periastron (Leahy & Kostka 2008; Islam & Paul 2014, and references therein).

GX 301-2 shows a strong 6.4-keV Fe K $\alpha$  fluorescent line, as well as many other fluorescent lines (Sarawat et al. 1996; Fürst et al. 2011; Suchy et al. 2012). The Fe K $\alpha$  fluorescent line is produced when the X-ray emission illuminates the surrounding gas; its intensity and spectral profile are important tools for the study of HMXBs (Torrejón et al. 2010; Giménez-García et al. 2015, and reference therein). For example, from the detection of a spectrally resolved Fe K $\alpha$  Compton shoulder at periastron, Watanabe et al. (2003) inferred an absorption column density of  $\approx 10^{24}$  cm<sup>-2</sup> and an electron temperature of  $\approx 0.5$  eV. The location of the Fe K $\alpha$  fluorescent region for GX 301-2 is still actively debated. Using spectral data from the *Advanced Satellite for Cosmology and Astrophysics* (ASCA), Endo et al. (2002) measured a Gaussian  $\sigma$  of  $\approx 40$ – $80$  eV for Fe K $\alpha$  and inferred an emission region within  $\approx 10^{10}$  cm (0.3 lt-s) of the neutron star. An *XMM-Newton* study (Fürst et al. 2011) did not reveal any significant time delays between the observed continuum and the reprocessed line emission, which implies a distance smaller than  $\approx 6 \times 10^{10}$  cm between the two sources of emis-

\* E-mail: jirenliu@nao.cas.cn

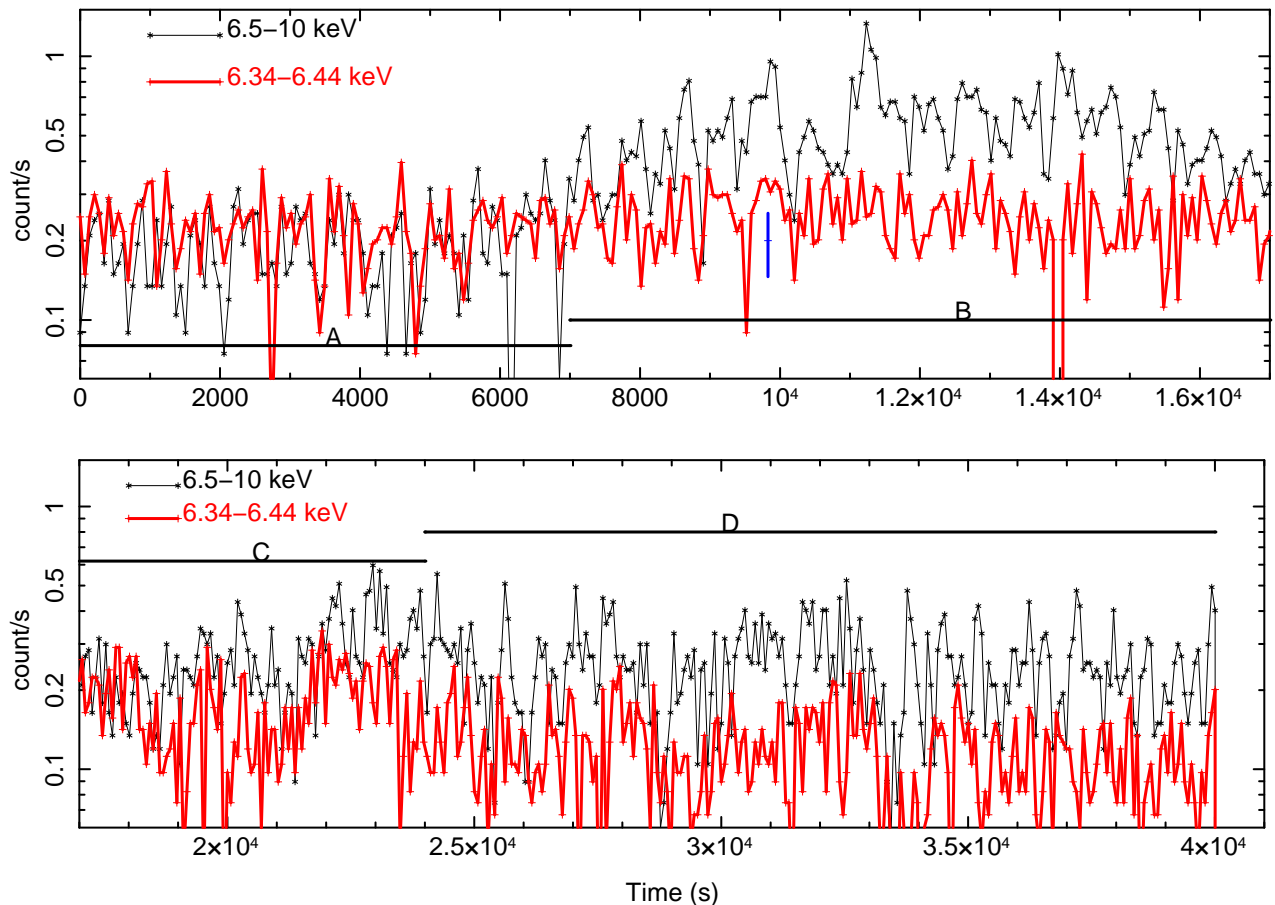


**Figure 1.** Light curves of the continuum-subtracted Fe  $K\alpha$  line (6.34–6.44 keV) and the continuum (6.5–10 keV), for the first 17 ks of the observation (top panel) and for the interval between 17–40 ks (bottom panel). The time resolution of the data points is 68 s = 0.1 times the pulse period. Letters indicate different sub-intervals of the observation, used for our timing and spectral analysis. The error bar plotted in the top panel at about  $10^4$  s represents a typical  $1\text{-}\sigma$  error, for a count rate of  $0.2\text{ ct s}^{-1}$ . We took half of the count rate within the 5.8–6 keV band as the continuum level for the Fe  $K\alpha$  line. We did not use the 7.0–7.2 keV band for the continuum estimate because it is contaminated by the Fe  $K\beta$  line.

sion. Instead, using *Suzaku* observations, Suchy et al. (2012) inferred a distance greater than  $\approx 2 \times 10^{13}$  cm (700 lt-s), based on the relatively flat phase profile of the line compared with that of the continuum. Despite this discrepancy in the proposed size of the line emission region, one thing that appeared well ascertained was that the Fe  $K\alpha$  line was less pulsed compared to the continuum (e.g. Fürst et al. 2011, and reference therein). In this paper, based on *Chandra X-ray Observatory* observations, we show that this is not always true: the Fe  $K\alpha$  line pulsates at times as strongly as the continuum.

## 2 X-RAY OBSERVATIONS

GX 301-2 has been observed with the High Energy Transmission Grating Spectrometers (HETGs) on board *Chandra* on three separate occasions between 2000 and 2002. One of those observations occurred around periastron passage (ObsID 2733, 2002 January 13, exposure time of 40 ks, start time at MJD 52,287.375): this is the dataset we are reporting on for this paper. More specifically, using the ephemeris and period derivative of Doroshenko et al. (2010), the start of the

*Chandra* observation is at orbital phase  $\phi = 0.998 \pm 0.003$ ; the duration of the *Chandra* observation is  $\Delta\phi = 0.011$ . Spectral analysis of this dataset has been reported elsewhere (Watanabe et al. 2003), but no timing analysis had been done.

*Chandra*'s HETGs consist of two sets of gratings: the Medium Energy Grating (MEG) and the High Energy Grating (HEG). We only used HEG data for this work, because of its better spectral resolution and larger collecting area in the Fe  $K\alpha$  band. We downloaded the data from the public archives, and reprocessed them with the *Chandra Interactive Analysis of Observations* (CIAO) software version 4.8 (Fruscione et al. 2006). We applied a barycenter correction with the CIAO tool *axbary*. We extracted the HEG source spectra from a  $2''$  region in the cross-dispersion direction with the TGCAT script (Huenemoerder et al. 2011).

In addition, we used one archival observation of GX 301-2 taken with the *Nuclear Spectroscopic Telescope Array* (*NuSTAR*) on 2015 October 4 (ObsID 30101042002). The system was observed at a binary phase  $\approx 0.9$ , relatively close to periastron. We extracted the source spectrum from a circle of  $1'.5$  radius, and the background spectrum from a

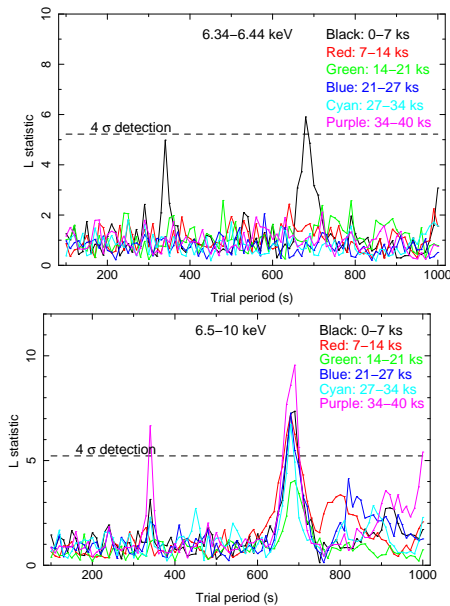


**Figure 2.** Top panel: statistical significance of the pulsation period for the Fe K $\alpha$  line during different sub-intervals of the *Chandra* observation; the pulse period is detected only in the first 7 ks. Bottom panel: statistical significance of the pulsation in the continuum. The dashed line shows  $4\sigma$  detection limit.

blank  $4'$  circle, using the *NuSTAR* Data Analysis Software (NuSTARDAS<sup>1</sup>).

We used the *sitar\_epfold\_rate* and *sitar\_pfold\_rate* tools within the SITAR<sup>2</sup> software package for timing analysis. We used the Interactive Spectral Interpretation System ISIS<sup>3</sup> (Houck & Denicola 2000) for spectral analysis of both the *Chandra* and *NuSTAR* data.

### 3 MAIN RESULTS

#### 3.1 Timing results

To investigate the physical changes in the system, we divided the 40-ks observation into four sub-intervals: 0–7 ks (henceforth labelled as interval A), 7–17 ks (B), 17–24 ks (C), and 24–40 ks (D), based on the flux levels of the Fe K $\alpha$  line (6.34–6.44 keV) and the continuum (6.5–10 keV). Half of the count rate in the 5.8–6 keV band was used for baseline continuum subtraction from the line flux. The light curves for the continuum-subtracted Fe K $\alpha$  line and the continuum are plotted in Figure 1, with a time resolution of 68 s = 0.1 times the pulse period.

In the first 7 ks of the observation, the fluxes from both the line and the continuum do not show any long-term trends, but both light curves are characterized by irregular flaring on timescales smaller than the pulse period (Figure 1). After 7 ks, in interval B, the continuum level increases; the average count rate is a factor of 3 higher than in interval A. This mini-flare is not to be confused with the so-called pre-periastron X-ray flare, which peaks at  $\phi \approx 0.90$ –

**Table 1.** Pulsed fraction for the four observation intervals

f	Interval A	Interval B	Interval C	Interval D
Fe K $\alpha$	0.29 $\pm$ 0.06	0.09 $\pm$ 0.05	0.13 $\pm$ 0.07	0.13 $\pm$ 0.06
Continuum	0.37 $\pm$ 0.06	0.23 $\pm$ 0.04	0.24 $\pm$ 0.06	0.33 $\pm$ 0.04
Faked Fe K $\alpha$	0.12 $\pm$ 0.03	0.12 $\pm$ 0.03	0.14 $\pm$ 0.04	0.17 $\pm$ 0.04

0.95 with an amplitude 10–20 times that of the quiet epochs (e.g. Islam & Paul 2014) and is one of the hallmarks of this HMXB. The average flux of the Fe K $\alpha$  line increases only by  $\approx 10\%$  between intervals A and B. In intervals C and D, both the continuum and the line flux decreased by similar amounts. Near the end of the observation, the continuum had settled to a level slightly higher than in interval A, while the Fe K $\alpha$  line was a factor of 2 fainter than in interval A.

We searched for periodicities in the Fe K $\alpha$  line and the continuum, using the epoch folding method between 100–1000 s with a step-size of 10 s and 10 phase bins for light curve (binned in 10 s) divided into 6.8 ks intervals. The L-statistic as defined in Davies (1990) is plotted in Figure 2. It obeys an F distribution with M-1 and N-M degrees of freedom, for N data points binned in M phase bins. The continuum shows the expected pulse periodicity (680 s) during the whole observation, while the Fe K $\alpha$  line shows significant periodicity (also at 680 s) only during interval A. A second peak at half of the pulsation period (340 s) is also significantly found for the line flux in interval A. The  $4\sigma$  detection limit ( $P(F \leq 5.22) = 99.99993\%$ , with 9 and 670 degrees of freedom, corrected for 91 searched periods) is shown as dashed line in Figure 2.

We folded the phase profile of line and continuum at different time intervals with 10 phase bins (Figure 3). For clarity the profiles of interval C (similar to those of interval D) are not plotted. We found that the phase profiles of Fe K $\alpha$  line and continuum look similar during interval A, with broad plateaux. For intervals B and D when no periodic pulsations of Fe K $\alpha$  line are detected, the folded phase profile of Fe K $\alpha$  line looks flat, as expected. The phase profiles of the continuum during intervals B and D show a main peak, similar to those reported in the literature (e.g. Fürst et al. 2011). Most importantly, the pulsating behaviour of the Fe K $\alpha$  line during interval A is a new discovery, not seen in previous observations.

The pulsed fractions defined as  $f = \frac{\max(p) - \min(p)}{\max(p) + \min(p)}$  are listed in Table 1. The pulsed fraction of the Fe K $\alpha$  line of interval A is larger than those of other intervals and is similar to those of the continuum. We simulated the pulsed fractions arising from intrinsic noise of data assuming a uniform phase profile with a Fe K $\alpha$  rate as the observed mean rate in the four intervals. The results for  $10^4$  runs are listed in Table 1. The fake pulsed fractions are similar to those of interval B, C, and D, but smaller than that of interval A, as expected.

#### 3.2 Spectral results

A study of the spectral properties of the same *Chandra* HEG observation was reported by Watanabe et al. (2003); however, the observation was divided simply into two halves of 20 ks each. Thus, the unusual pulsating behaviour of the Fe K $\alpha$  line in the first 7 ks, and its subsequent sudden disap-

<sup>1</sup> <https://heasarc.gsfc.nasa.gov/docs/nustar/analysis/>

<sup>2</sup> <http://space.mit.edu/cxc/analysis/SITAR/distrib.html>

<sup>3</sup> <http://space.mit.edu/cxc/isis/>

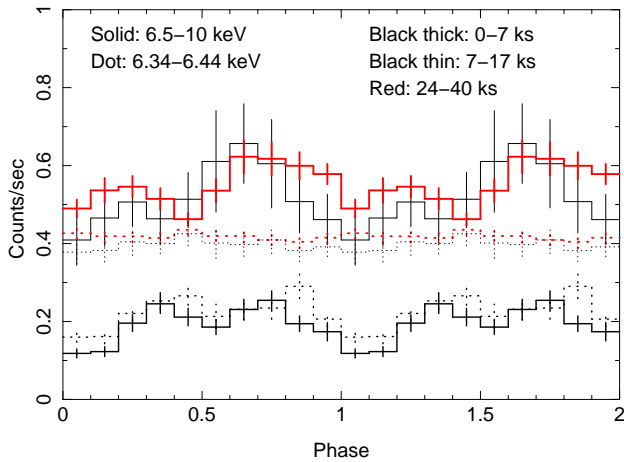


**Figure 3.** Phase profiles of the Fe  $K\alpha$  line and the continuum for sub-intervals A (0–7 ks), B (7–17 ks), and D (24–40 ks). For clarity, the pulse profiles of the Fe  $K\alpha$  line for intervals B and D have been up-shifted by 0.15 and 0.3, respectively; the continuum profile of interval D has also been up-shifted by 0.3.

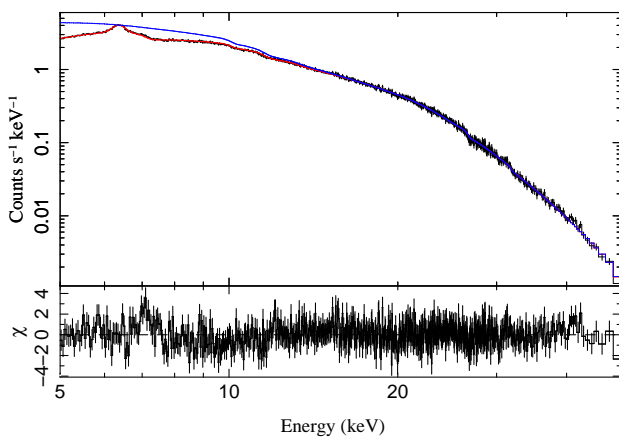


**Figure 4.** *NuSTAR* FPMA (focal plane module A) spectrum of GX 301-2 re-binned with a minimum S/N of 10. The blue line shows an unabsorbed power-law with a high-energy cutoff fitted to energies between 15 and 50 keV. The red line shows an absorbed power-law fitted to energies between 5 and 50 keV, plus a Gaussian line. The residuals of the absorbed power-law plus Gaussian model are plotted in the bottom panel.

pearance, went unnoticed. We analyzed the spectra of the four intervals A, B, C, and D separately (Figure 5). In all four intervals (but especially in interval A), the spectrum showed a strong Compton shoulder red-ward of the narrow Fe  $K\alpha$  line, which implies a non-negligible contribution of the scattered component to the continuum.

Recent studies (e.g. [Martínez-Núñez et al. 2017](#)) have shown that stellar winds from massive stars are composed of inhomogeneous clumps. The X-ray spectrum of a source seen through a clumpy medium is very different from that of a source seen through a smooth one ([Liu & Li 2014](#)). For a clumpy distribution, there are many lower-density gaps between the clouds, in which low-energy X-ray photons (1–5 keV) can pass without being heavily absorbed. The clumpier the gas, the stronger the scattered low-energy emission. This

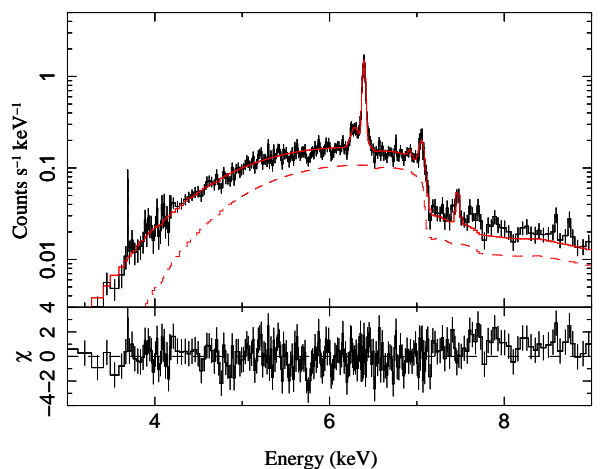
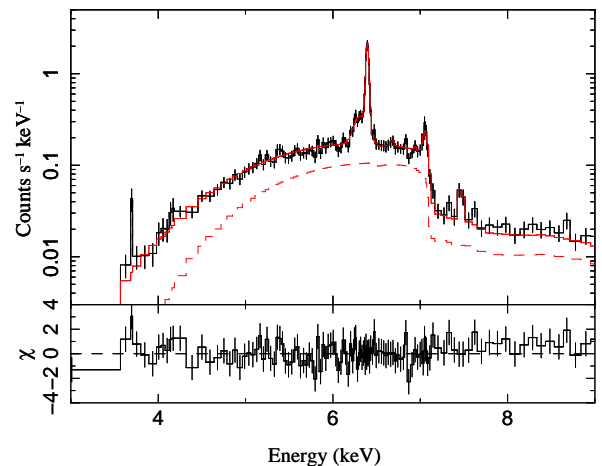
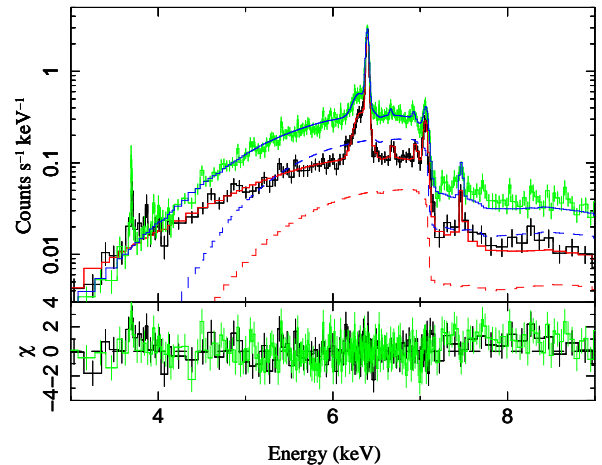


**Figure 5.** Top panel: *Chandra* HEG spectrum in interval A (black data points and residuals) and B (green data points and residuals). Both spectra are fitted with a clumpy torus model plus transmitted intrinsic continuum and a set of 7 Gaussian lines. The model for the interval-A spectrum is over-plotted as a solid red histogram, while the model for interval B is a solid blue histogram. The transmitted intrinsic components of both models are also plotted as dashed histograms (red for interval A and blue for interval B). The residuals  $\chi$  are defined as the difference between data and model, divided by the data error. See Table 2 for the best-fitting spectral parameters and errors. Middle panel: *Chandra* HEG spectrum and model residuals for interval C. The model (solid red histogram) is the same as for interval A. The dashed red histogram shows the transmitted continuum. Bottom panel: as in the middle panel, but for interval D.

is likely why the observed low-energy spectra of GX 301-2 have generally been modelled as a partial-covering power-law (e.g. Fürst et al. 2011). It is a simple phenomenological model to reproduce the scattered continuum component from a clumpy material; instead, a smooth absorbing medium with the same column density ( $\approx 10^{24}$  cm $^{-2}$ ) would completely absorb photons below  $\approx 3$  keV.

While many HMXBs show photoionization lines, the spectrum of GX 301-2 is quite different. It is highly attenuated and dominated by neutral-like fluorescent lines (e.g. Fürst et al. 2011). Such a reprocessing by neutral medium is similar to the process occurring in the clumpy tori of AGN. Therefore, we choose to fit the continuum of GX 301-2 with the ‘‘clumpy torus’’ (Ctorus<sup>4</sup>) model of Liu & Li (2014), which is implemented as a table model in ISIS. Ctorus calculates the spectrum of scattered X-ray emission emerging from a clumpy torus, given an input power-law spectrum with a photon index  $\Gamma$  between 1.5 and 2.5. The model includes the absorbed intrinsic continuum (transmitted component) and the scattered component. The normalization of the scattered component is determined by the normalization of the input power law ( $K_{\text{pl}}$ ). The column densities seen by the transmitted and scattered components ( $N_{\text{H}}^{\text{T}}$  and  $N_{\text{H}}^{\text{R}}$ , respectively; Table 2) are treated as independent fit parameters, because the absorbing column density along our line of sight may be different from the average column density through the scattering material. The clumpiness is represented by the average cloud number along any line of sight ( $N$ , ranging between 2 and 10, the smaller the  $N$ , the more clumpy the gas) and the filling factor (assumed here to be 0.1). The densities and sizes of clumps are determined by  $N_{\text{H}}^{\text{R}}$ ,  $N$ , and the filling factor (see Liu & Li 2014, for more details). We assumed an inclination angle of  $90^\circ$  (edge-on) to approximate a spherical geometry.

When fitting the spectra of GX 301-2, we found that the best-fitting photon indices always reach the lower limit of the model,  $\Gamma = 1.5$ . Therefore, we fixed the photon index to 1.5. To verify that this is a reasonable approximation, we extracted and analysed an archival *NuSTAR* spectrum taken at an orbital phase of  $\approx 0.9$  as mentioned in §2. We first fitted the spectrum between 15 and 50 keV using a power-law with a smoothed high-energy cutoff model (eq. 2 in La Barbera et al. 2001). We found a photon index of  $1.39 \pm 0.08$  with a cutoff energy of  $23.9 \pm 0.4$  keV and a folding energy of  $8.7 \pm 0.3$  keV (blue line in Figure 4). The reduced  $\chi^2 = 1.0$ . Then we fitted the spectrum between 5 and 50 keV using an absorbed power-law with high-energy cutoff, plus a Gaussian line around 6.4 keV, and found a photon index of  $1.35 \pm 0.03$  with a cutoff energy of  $23.7 \pm 0.3$  keV, a folding energy of  $8.6 \pm 0.2$  keV, a line with centroid of  $6.37 \pm 0.01$  keV and  $\sigma$  of  $50_{-50}^{+30}$  eV, and a column density of  $1.4 \pm 0.1 \times 10^{23}$  cm $^{-2}$  (red line in Figure 4). The reduced  $\chi^2 = 1.1$ . The residuals are mainly around 7.1 keV (Fe K $\beta$  line). Therefore, a photon index of 1.5 is not far from those obtained from *NuSTAR* data. We note that our main results are not affected by the exact slope of the power-law used to approximate the continuum.

Ctorus model has also a fluorescent component, however, it does not include the Compton shoulder of the Fe

K $\alpha$  line currently. The rest-frame energies adopted for the fluorescent lines also have some discrepancies with those measured in the laboratory (Bearden 1967), which makes the usage of the fluorescent component not straight forward. Therefore, we use Gaussian to model the emission lines. As the narrow Fe K $\alpha$  line is very close to 6.4 keV, we use two Gaussian (Table 2) with centroids at 6.404 keV and 6.391 keV, to represent the K $\alpha$  1 and K $\alpha$  2 doublet (Bearden 1967). The intensity ratio between K $\alpha$  1 and K $\alpha$  2 is set to 2:1, and their velocity shifts and Gaussian widths are fixed to be the same for the two components. The neutral Fe K $\beta$  line is also modelled as a Gaussian (Table 2) centered at 7.058 keV. We add another Gaussian with an energy around 6.3 keV to represent the Compton shoulder. In addition, we find relatively weak line features around 6.7 keV, 6.9 keV, and 7.5 keV, which we interpret as He-like Fe, H-like Fe, and neutral Ni K $\alpha$  lines. We also modelled them as Gaussian (Table 2) with a fixed width of 1 eV.

First, we fitted the spectrum from interval A (Table 2 and black data points in the top panel of Figure 5). We found that the direct power-law component contributes only  $\approx 1/3$  of the observed continuum emission around 6.5–9 keV; the rest comes from the scattered continuum. If both the Fe K $\alpha$  line and the continuum are dominated by photons scattered in Compton-thick gas, this could explain the similarity of their phase profiles; however, the location and geometry of the scattering medium must be such as to preserve the pulsation signal.

For interval B, first we tried freezing the power-law normalization and the scattering column density in Ctorus to the best-fitting values found for interval A, and only allowed the absorbing column density as a free parameter. We wanted to test the scenario that the increase in the observed continuum flux was solely due to a decrease in the absorbing column density. With this assumption, we get a column density of  $N_{\text{H}}^{\text{T}} = (8.9 \pm 0.1) \times 10^{23}$  cm $^{-2}$  and  $\chi^2_{\nu} = 2.3$ . The model does not do a good job of reproducing the continuum at the low- and high-energy ends. We obtain a better fit ( $\chi^2_{\nu} = 1.26$ ; green data points in the top panel of Figure 5) when we thaw the normalization of the intrinsic power-law and the reprocessing column density. The power-law normalization is about twice the value in interval A (Table 2); the transmitted component now accounts for about half of the observed continuum flux above 6.5 keV. If the increase of the intrinsic luminosity is real, and no other changes occur in the distribution of the scattering medium, we would expect to see a corresponding increase of the fluxes from the Fe lines; however, all line fluxes are found to be similar between intervals A and B, within the uncertainties (Table 2). What does change in the line properties is the loss of the pulsation signal.

Finally, we fitted the same model to the spectra of intervals C (Figure 5, middle panel) and D (Figure 5, bottom panel). The trend for these late intervals is that the normalization of the intrinsic power-law emission decreases, and the scattering column density also decreases. The ratio between the measured fluxes of the Compton shoulder and of the Fe K $\alpha$  line is about 35% and 32% for intervals A and B, decreasing to about 29% and 17% for intervals C and D, consistent with the reduced scattering column density. The combined result of both changes is that the contribution of the absorbed intrinsic emission is larger than half of the ob-

<sup>4</sup> <https://heasarc.gsfc.nasa.gov/xanadu/xspec/models/Ctorus.html>

**Table 2.** Best-fitting parameters for our model (Ctorus + seven Gaussian lines) in the four sub-intervals of the *Chandra* observation. Errors are 90% confidence levels for one interesting parameter.

Parameter	Interval A	Interval B	Interval C	Interval D
Ctorus				
$K_{\text{pl}}$ (photons keV <sup>-1</sup> cm <sup>-2</sup> s <sup>-1</sup> at 1 keV)	3.8±0.6	7.9±2.0	2.4±0.7	1.8±0.3
$N^a$	3.5±0.6	5.8±0.7	> 6.8	> 6.8
$N_{\text{H}}^{\text{T}}$ (10 <sup>24</sup> cm <sup>-2</sup> )	1.5±0.5	1.3±0.1	1.0±0.1	0.9±0.1
$N_{\text{H}}^{\text{R}}$ (10 <sup>24</sup> cm <sup>-2</sup> )	1.6±0.3	1.5±0.1	0.9±0.1	0.8±0.1
Neutral Fe K $\alpha$ doublet				
$E_1$ (keV)			[6.404]	
$E_2$ (keV)			[6.391]	
$\Delta v_{\text{K}\alpha}$ (km s <sup>-1</sup> )	180±60	240±30	210±60	240±60
$\sigma_1 = \sigma_2$ (eV)	4.8±3.1	8.7±1.8	7.0±2.2	7.9±2.0
$N_1 + N_2$ (10 <sup>-3</sup> photons cm <sup>-1</sup> s <sup>-1</sup> )	10.0±0.6	11.2±0.6	8.2±0.7	5.8±0.3
EW (keV)	0.52±0.03	0.28±0.02	0.38±0.03	0.36±0.02
Neutral Fe K $\beta$				
$E_3$ (keV)			[7.058]	
$\Delta v_{\text{K}\beta}$ (km s <sup>-1</sup> )	-180±180	-60±30	-120±330	-150±240
$\sigma_3$ (eV)	19±8	23±5	24±13	26±8
$N_3$ (10 <sup>-3</sup> photons cm <sup>-1</sup> s <sup>-1</sup> )	2.6±0.4	3.1±0.4	2.0±0.4	1.6±0.3
Neutral Fe K $\alpha$ Compton shoulder				
$E_4$ (keV)	6.32±0.01	6.30±0.02	6.31±0.03	6.29±0.01
$\sigma_4$ (eV)	63±10	63±13	60±18	37±12
$N_4$ (10 <sup>-3</sup> photons cm <sup>-1</sup> s <sup>-1</sup> )	3.5±0.6	3.6±0.6	2.4±0.9	1.0±0.3
He-like Fe K $\alpha$				
$E_5$ (keV)	6.68±0.01	6.66±0.02	6.68±0.05	6.69±0.10
$\sigma_5$ (eV)			[1]	
$N_5$ (10 <sup>-3</sup> photons cm <sup>-1</sup> s <sup>-1</sup> )	0.3±0.2	0.3±0.2	0.1±0.2	0.0±0.1
H-like Fe K $\alpha$				
$E_6$ (keV)	6.95±0.01	6.93±0.02	6.95±0.05	6.93±0.03
$\sigma_6$ (eV)			[1]	
$N_6$ (10 <sup>-3</sup> photons cm <sup>-1</sup> s <sup>-1</sup> )	0.4±0.2	0.4±0.2	0.1±0.3	0.2±0.1
Neutral Ni K $\alpha$				
$E_7$ (keV)	7.47±0.02	7.47±0.01	7.47±0.01	7.47±0.01
$\sigma_7$ (eV)			[1]	
$N_7$ (10 <sup>-3</sup> photons cm <sup>-1</sup> s <sup>-1</sup> )	0.7±0.3	1.0±0.3	0.8±0.3	0.5±0.2
$\chi^2_{\nu}$ ( $\chi^2/\text{dof}$ )	1.17 (112/96)	1.26 (301/238)	0.93 (98/105)	1.31 (305/233)
$L_{2-10}^b$ (10 <sup>37</sup> erg s <sup>-1</sup> )	3.1±0.5	6.4±1.6	1.9±0.6	1.5±0.3

Notes: <sup>a</sup>: clumpiness parameter (average number of clouds along any line of sight); <sup>b</sup>: 2–10 keV de-absorbed luminosity of the intrinsic power-law component;  $N_i$  is the normalization for corresponding Gaussian line.

served continuum flux above 6.5 keV for intervals C and D. The fluorescence line fluxes also decrease, either because of the reduction in the intrinsic continuum flux, or because of the decrease in the scattering optical depth, or both.

The measured offsets of the Fe K $\alpha$  line from those of totally neutral Fe are very small; it indicates that the Fe K $\alpha$  photons are mostly due to nearly neutral Fe ions. This is consistent with the relatively low temperature found by [Watanabe et al. \(2003\)](#). The best-fitting Gaussian width  $\sigma$  (defined as  $\sigma = 1/2.35$  of the full-width-half-maximum, FWHM) of the Fe K $\alpha$  line is around 5–9 eV during the four observational intervals. These values are consistent with those independently reported by

[Tzanavaris & Yaqoob \(2018\)](#), also based on *Chandra* data. Instead, they are smaller than those reported in previous studies (e.g. [Endo et al. 2002](#); [Fürst et al. 2011](#)), as mentioned in Section 1. The discrepancy is most likely due to the higher spectral resolution of *Chandra* HEG. As the natural width of the Fe K $\alpha$  line is FWHM  $\approx 3$  eV, the Gaussian widths fitted in our spectral models are consistent with a velocity broadening ( $\approx 1/2$  FWHM) of  $\approx 200$ – $400$  km s<sup>-1</sup>. The fitted values of  $\sigma$  for the Fe K $\beta$  line are a little higher than those of the Fe K $\alpha$  line; those measurements may be affected by the Fe absorption edge near 7.1 keV. The inferred equivalent widths (EW) of the Fe K $\alpha$  line and the absorption-corrected intrinsic power-law luminosities for the

four intervals are also listed in Table 2. The smaller EW of interval B is due to the larger continuum level of interval B, compared with interval A.

The fitted  $N_{\text{H}}^{\text{T}}$  and  $N_{\text{H}}^{\text{R}}$  are similar and decrease from interval A to D. The fitted averaged cloud number increases from interval A to D. It seems that from interval A to D, the medium is changing from a clumpy dense region to a less-clumpy less-dense region. We note that the Ctorus model used has some deficiencies, for example, the input power-law does not include a high energy cutoff, as is required for GX 301-2; the photon index is limited to 1.5-2.5; the torus geometry may not represent the true cases. Further model developments are needed to obtain more conclusive results.

#### 4 DISCUSSION AND CONCLUSIONS

The key new result of this paper is that we detected a pulsating Fe K $\alpha$  line with the same period as the continuum, during the first 7 ks (interval A) of a *Chandra* observation of GX 301-2. The phase profile of the Fe K $\alpha$  line was also similar to that of the continuum. The pulsation signal of the Fe K $\alpha$  line then disappeared; at that time, the continuum flux increased by a factor of 3 and kept its pulsation profile; the line flux increased only by about 10%.

X-ray fluorescence lines are one of the hallmarks of neutron star HMXBs (*e.g.*, Leahy & Creighton 1993; Basko 1978; Hatchett & McCray 1977); they may be formed in many locations: in the accretion column, on the surface of the donor star or of an accretion disk, in the stellar wind, or in an accretion stream, shell or wake. Usually, the line emission is not pulsed (*e.g.*, Beri et al. 2015; Suchy et al. 2012; Wilkinson et al. 2011; Lei et al. 2009; Paul et al. 2002). A few well-studied exceptions, where fluorescent line emission from iron, oxygen and/or neon is pulsed, are 4U 1626–67 (Beri et al. 2015; Schulz et al. 2001; Angelini et al. 1995), Hercules X-1 (Vasco et al. 2013; Zane et al. 2004; Choi et al. 1994), and GX 1+4 (Yoshida et al. 2017a,b; Kotani et al. 1999).

GX 301-2 was one of the X-ray pulsars in which the pulsed fraction of the Fe K $\alpha$  line was always absent or much smaller than the pulsed signal in other energy bands; this was explained as the effect of smearing of the pulsed signal in an isotropic line-emitting region around the neutron star (Tashiro et al. 1991; Endo et al. 2002; Fürst et al. 2011). Instead, we have now shown that at some epochs, the pulsed fraction of the line is as high as that of the continuum. Thus, the simplest qualitative explanation of this finding is that during those epochs, the pulsating Fe K $\alpha$  line originates in an anisotropic gas structure, illuminated by the pulsed emission of the neutron star. More remarkably, we have shown that the line pulsation disappears at a phase  $\phi = 0.000 \pm 0.003$  (extrapolating from the ephemeris and period derivative solution of Doroshenko et al. 2010).

The inferred column density of the scattering medium responsible for the K $\alpha$  fluorescence lines (inferred from the relative strength of the K $\alpha$  Compton shoulder), and for the scattered continuum (inferred from broad-band spectral modelling) are similar, that is  $\approx 1.5 \times 10^{24} \text{ cm}^{-2}$ . Such a high column density cannot be produced by the quasi-isotropic stellar wind of a super-giant donor, but can be reached in the transient accretion stream formed between the donor

star and the neutron star near periastron (Stevens 1988). Evidence for the existence of this dense stream flow comes from studies of optical lines (Kaper et al. 2006), and the recurrent pre-periastron X-ray flare (Leahy & Kostka 2008, and references therein). When the neutron star enters and leaves the accretion stream, an anisotropic configuration will be formed. Specifically, the *Chandra* observation studied in this work was taken shortly after the flare; in the accretion stream scenario, it might correspond to the phase when the neutron star leaves the accretion stream. The illumination of the anisotropic stream distribution would produce the pulsating Fe K $\alpha$  line. When the neutron star moves further away from the stream, the contribution of the pulsating Fe K $\alpha$  line becomes less important. Such a scenario also predicts a pulsating Fe K $\alpha$  line when the neutron star enters the accretion stream, *i.e.*, before the X-ray flare. Moreover, the pulsating behaviour should repeat at similar phases every orbital cycle. Such a scenario can be tested with future observations.

Another possible anisotropic structure is the surface of the donor star. At periastron, the donor star subtends a solid angle  $\Omega_{\text{p}} \approx 1.88 \text{ sr}$ , that is, it is seen by the neutron star with an apex half-angle  $\theta \approx 45^\circ$ . Thus, for a moderate misalignment between the beam of X-ray emission and the normal to the orbital plane, the beamed X-ray emission of the neutron star could directly illuminate the surface of the donor star, and produce the pulsating Fe K $\alpha$  line. As the neutron star moves away from periastron, the solid angle subtended by the donor star decreases. At apastron, the subtended solid angle is only  $\Omega_{\text{a}} \approx 0.22 \text{ sr}$ , corresponding to a half-angle  $\theta \approx 15^\circ$ . In this scenario, we suggest that the disappearance of the pulsating line signal corresponds to the X-ray beam missing the stellar surface. Such scenario predicts that the pulsating phenomenon repeats periodically at periastron, and can also be tested with future observations.

The phase profile of the Fe K $\alpha$  line of GX 301-2 during interval A is quite different from those reported in the literature for other sources with pulsating line emission. For example, the phase profile of the Fe K $\alpha$  line from Her X-1 shows a sharp minimum around the continuum peak, which might indicate a hollow cone of the accretion structure (Vasco et al. 2013). The O VII line fluxes of 4U 1626–67 show a variation stronger than that of the continuum, which could be due to variable illumination of the warped region of an accretion disk (Beri et al. 2015). In contrast, the phase profile of the Fe K $\alpha$  line of GX 301-2 during interval A is similar to that of the continuum. It indicates that a major part of the observed continuum might come from the Compton-thick medium producing the Fe K $\alpha$  line, as evidenced by the spectral modelling in §3.2.

In principle, even a homogeneous, spherically symmetric scattering medium illuminated by a central X-ray pulsar can produce a fluorescent signal that appears pulsed to the distant observer, because of the finite-light-speed effect (Yoshida et al. 2017b). However, the characteristic size of the medium for this effect to be significant is of order of the pulsar spin period times the speed of light. In the case of GX 301-2, that would require a scattering medium with a size  $\sim 10^{13} \text{ cm}$ , implausibly larger than the binary system itself.

The possibility that the observed continuum could have a significant contribution from reprocessed emission may change the interpretation of the time delays between the

line and continuum. Using *XMM-Newton* data, Fürst et al. (2011) found no time delays between Fe  $K\alpha$  line and continuum in the time range of 2–5,000 s, and they inferred a fluorescent region smaller than 2 lt-s ( $6 \times 10^{10}$  cm). However, if a major part of observed continuum come from scattering, far from the neutron star surface, the lack of relative time delays would no longer constrain the size of the region. A reanalysis of *XMM-Newton* data is needed to check this possibility.

Another way to constrain the region of the fluorescent lines is through their velocity broadening. Thanks to the *Chandra* HEG resolution, we have shown that typical velocity broadening of the Fe  $K\alpha$  line is  $\approx 200$ – $400$  km s $^{-1}$ , a few times lower than previously inferred. This is comparable to the typical terminal velocity of the stellar wind and the ballistic motion of an accretion stream. If the broadening is due to gas in virial motion, such velocities would correspond to distances  $\sim 5 \times 10^{10}$ – $2 \times 10^{11}$  cm for a neutron star of  $1.5 M_{\odot}$ , similar to the accretion radius of GX 301-2 ( $\sim 10^{11}$  cm). Such a relatively large scale is consistent with fluorescence lines from cool and nearly neutral Fe ions. We note that it is much larger than the magnetosphere of a neutron star even with a field of  $10^{14}$  G ( $4 \times 10^9$  cm). On the other hand, the fluorescent region can not be larger than the light travel distance of a significant fraction of the pulse period (e.g., 100 ls), otherwise the pulsation signal would be smeared out. In principle, any temporary anisotropic gas structure on scales of  $\sim 10^{11}$  cm with enough covering factor, like a torus or a warped accretion disk, could be invoked to explain the pulsating Fe  $K\alpha$  line. Such gas structures are likely caused by the dynamical interaction between the donor star and the neutron star near periastron. Detailed hydrodynamical simulations are needed to test the existence of such structures.

The increase in the observed continuum after the first 7 ks of the observation, accompanied by the non-increase of the line emission and the disappearance of the pulsed line signal remain puzzling, and can be due to a combination of increased intrinsic emission, decreased absorption column density along our line of sight, and decreased column density of the scattering medium. Simultaneous observations in wide X-ray bands are needed to disentangle these effects. Nonetheless, using only the *Chandra* HEG data, we have already shown a decreasing trend in the column density of the scattering medium in the second half of the observation. This is seen both from our broad-band continuum modelling, and from the progressively lower flux ratio between the Compton shoulder and the Fe  $K\alpha$  line.

## ACKNOWLEDGEMENTS

We thank our anonymous referee for valuable suggestions that improve the work significantly, and Youjun Lu for helpful discussions. JL is supported by NSFC grant 11203032. This research is based on data obtained from the *Chandra* Data Archive. We made use of software obtained from the High Energy Astrophysics Science Archive Research Center (HEASARC), a service of the Astrophysics Science Division at NASA/GSFC and of the Smithsonian Astrophysical Observatory's High Energy Astrophysics Division.

## REFERENCES

- Angelini L., White N.E., Nagase F., Kallman T.R., Yoshida A., Takeshima T., Becker C., Paerels F., 1995, *ApJ*, 449, L41
- Basko M.M., 1978, *ApJ*, 223, 268
- Bearden J.A., 1967, *Rev. Mod. Phys.*, 39, 78
- Beri A., Paul B., Dewangan G.C., 2015, *MNRAS*, 451, 508
- Choi C.S., Nagase F., Makino F., Dotani T., Kitamoto S., Takahama S., 1994, *ApJ*, 437, 449
- Davies S.R., 1990, *MNRAS*, 244, 93
- Doroshenko V., Santangelo A., Suleimanov V., Kreykenbohm I., Staubert R., Ferrigno C., Klochkov D., 2010, *A&A*, 515, 10
- Endo T., Ishida M., Masai K., Kunieda H., Inoue H., Nagase F., 2002, *ApJ*, 574, 879
- Evangelista Y., et al., 2010, *ApJ*, 708, 1663
- Fruscione A., et al. 2006, *Proceedings of the SPIE*, 6270, 1
- Fürst F., et al., 2011, *A&A*, 535, 9
- Giménez-García A., Torrejón J.M., Eikmann W., Martínez-Núñez S., Oskina L.M., Rodes-Roca J.J., Bernabéu G., 2015, *A&A*, 576, 108
- Göğüş E., Kreykenbohm I., Belloni T.M., 2011, *A&A*, 525, 6
- Goldstein G., Huenemoerder D.P., Blank D., 2004, *AJ*, 127, 2310
- Hatchett S., McCray R., 1977, *ApJ*, 211, 552
- Houck J.C., Denicola L.A., 2000, *ASPC*, 216, 591
- Huenemoerder D.P., et al., 2011, *AJ*, 141, 129
- Ikhsanov N. R., Finger, M. H. 2012, *ApJ*, 753, 1
- Islam N., Paul B., 2014, *MNRAS*, 441, 2539
- Kaastra J.S., Mewe R., 1993, *A&AS*, 97, 443
- Kaper L., van der Meer A., Najjarro F., 2006, *A&A*, 457, 595
- Koh D.T., et al., 1997, *ApJ*, 479, 933
- Kotani T., Dotani T., Nagase F., Greenhill J.G., Pravdo S.H., Angelini L., 1999, *ApJ*, 510, 369
- La Barbera, A., Burderi, L., Di Salvo, T., Iaria, R., Robba, N. R., 2001, *ApJ*, 553, 375
- Leahy D.A., Creighton J., 1993, *MNRAS*, 263, 314
- Leahy D.A., Kostka M., 2008, *MNRAS*, 384, 747
- Lei Y.-J., Chen W., Qu J.-L., Song L.-M., Zhang S., Lu Y., Zhang H.-T., Li T.-P., 2009, *ApJ*, 707, 1016
- Liu Y., Li X., 2014, *ApJ*, 787, 52
- Liu J., Liu Y., Li X., Xu W., Gou L., Cheng C., 2016, *MNRAS*
- Martínez-Núñez S., et al., 2017, *SSRev*, 212, 59
- Paul B., Dewangan G.C., Sako M., Kahn S.M., Paerels F., Liedahl D., 2002, *Proceedings of the IAU 8th Asian-Pacific Regional Meeting (Tokyo)*, Eds. S. Ikeuchi, J. Hearnshaw, and T. Hanawa, Vol. 2, p. 355
- Saraswat P., et al., 1996, *ApJ*, 463, 726
- Sato N., et al., 1986, *ApJ*, 304, 241
- Schulz N.S., Chakrabarty D., Marshall H.L., Canizares C.R., Lee J.C., Houck J., 2001, *ApJ*, 563, 941
- Stevens I.R., 1988, *MNRAS*, 232, 199
- Suchy S., Fürst F., Pottschmidt K., Caballero I., Kreykenbohm I., Wilms J., Markowitz A., Rothschild R.E., 2012, *ApJ*, 745, 124
- Tashiro M., Makishima K., Ohashi T., Sakao T., Sansom A.E., 1991, *MNRAS*, 252, 156
- Torrejón J.M., Schulz N.S., Nowak M.A., Kallman T.R., 2010, *ApJ*, 715, 947
- Tzanavaris P., Yaqoob T., 2018, *arXiv:1801.08544*
- Vasco D., Staubert R., Klochkov D., Santangelo A., Shakura N., Postnov K., 2013, *A&A*, 550, 111
- Watanabe S., et al., 2003, *ApJ*, 597, L37
- Wilkinson T., Patruno A., Watts A., Uttley P., 2011, *MNRAS*, 410, 1513
- Yoshida Y., Kitamoto S., Hoshino A., 2017, *ApJ*, 849, 116
- Yoshida Y., Kitamoto S., Suzuki H., Hoshino A., Naik S., Jaisawal G.K., 2017, *ApJ*, 838, 30
- Zane S., Ramsay G., Jimenez-Garate M.A., Willem den Herder J., Hailey C.J., 2004, *MNRAS*, 350, 506